Spectroscopic Absorption Measurements of an Iron Plasma

P. T. Springer,(1) D. J. Fields,(1) B. G. Wilson,(1) J. K. Nash,(1) W. H. Goldstein,(1) C. A. Iglesias,(1) F. J. Rogers,(1) J. K. Swenson,(1) M. H. Chen,(1) A. Bar-Shalom,(2) and R. E. Stewart(1)

(1)*Lawrence Livermore National Laboratory, P.O. Box 808, Livermore, California 94550*
(2)*Nuclear Research Center Negev, P.O. Box 9001, Beer-Sheva 84190, Israel*

(Received 14 September 1992)

The first quantitative measurement of photoabsorption in the region determining the Rosseland and Planck mean opacities is obtained for a well-characterized, radiatively heated iron plasma using new techniques and instrumentation. The plasma density and temperature are simultaneously constrained with high accuracy, allowing unambiguous comparisons with opacity models used in modeling radiative transfer in equilibrium astrophysical and laboratory plasmas. The experimental Rosseland and Planck group means are constrained to an accuracy of 15%.

PACS numbers: 52.25.Nr, 44.40.+a, 52.50.Jm, 52.70.La

The radiative properties of hot, dense matter are crucial to understanding systems ranging from stellar interiors to inertial confinement fusion plasmas [1]. Models for photoabsorption are complex, requiring knowledge of atomic structure, of level populations, of spectral line shapes, and of plasma interactions. The models often make simplifying assumptions and approximations due to the enormous amount of atomic data required, and to the intractable nature of the many-body problem. In view of their complexity, their widespread utility, and their compromises, it is crucial to validate opacity models through well-characterized laboratory measurements.

Previous high precision photoabsorption measurements probed regions accessible to crystal spectroscopy [2-6]. While these measurements benefited opacity models, they did not access the spectral region lying near the peak of the Planck distribution, which dominates the radiative energy flow. Recent x-ray ultraviolet (XUV) measurements [7] have shown the gross character of photoabsorption in this band. There, low precision was sufficient, allowing the use of multiple shots and complex hydrodynamic simulations as a guide to temperature and density. However, opacity models depend critically upon plasma conditions. Consequently, benchmark experiments require complete and precise characterization as well as precise transmission data. In this Letter we describe new instrumentation and techniques that have allowed us to extend high precision photoabsorption measurements into these soft-x-ray and XUV spectral regimes that dominate radiative transport for these equilibrium laboratory plasmas. In the present work, the sample is spatially imaged to maximize the precision of the transmission measurement, while simultaneous spectroscopic measurements accurately constrain the plasma conditions. These techniques lead to the first accurate measurements of Planck and Rosseland group mean opacities.

The experimental methodology is similar to earlier work [2-5]. The NOVA laser at Lawrence Livermore National Laboratory is used to indirectly heat a tamped thin foil sample consisting of 132 $\mu\mathrm{g\,cm}^{-2}$ of iron mixed with 55 $\mu\mathrm{g\,cm}^{-2}$ of sodium fluoride. The 1000×300-μm foil is sandwiched between two larger 100-$\mu\mathrm{g\,cm}^{-2}$ layers of Lexan, that act as a tamper and maintain a uniform spatial density in the heated sample. The 16-kJ, 353-nm heating laser has a duration of 1 ns and creates x rays that radiatively heat the sample and cause it to expand. We depart from the method of point projection spectroscopy [2-5], and instead use grating spectrometers, time-gated detectors, pinhole imaging, and large area backlights. These new techniques allow measurements of the specific brightness of the sample and backlight emitters. In addition, the emission backgrounds are reduced and quantified, permitting accurate XUV measurements on higher temperature plasma.

The experimental setup is illustrated in Fig. 1. The tamped target is viewed edge on by an XUV spectrometer through 300 μm of the foil, and is illuminated by a uniform 1 mm^2 area x-ray backlight, created when a NOVA

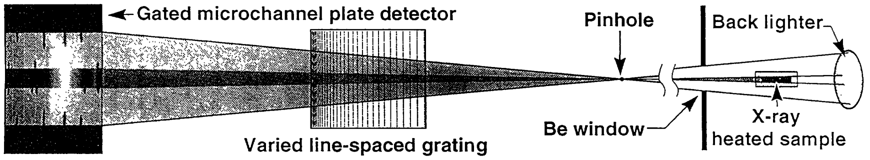

FIG. 1. Schematic drawing of the experimental setup. The radiatively heated Fe plus NaF sample is viewed edge on with the XUV spectrometer, with pinhole imaging, a gated microchannel plate detector, and is backlighted by a laser irradiated gold foil. X rays that pass through and to the side of the plasma are compared to obtain the plasma transmission.

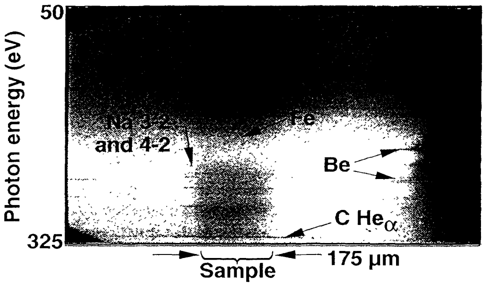

FIG. 2. Spatially resolved (left to right) and spectrally dispersed from 50 to 325 eV (top to bottom) x-ray transmission image of the Fe/NaF sample. Iron $n=3$ to $n=4$ and 5 absorption features appear in the image center as dark bands traversing the plasma. The sodium and fluorine lines are most clearly visible on the left-hand edge of the sample. Beryllium and carbon lines are also observed from the aperture and the Lexan tamper.

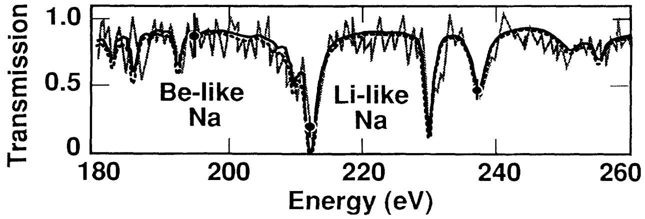

FIG. 3. Sodium transmission data (gray line) and OPAL calculations with MCDF atomic data performed at measured density of 0.008 36 g cm^{-3}, 91 wt% NaF, and temperatures of 59 eV (solid line) and 57 eV (dotted line). The areal density is 219 μg cm^{-2}. The data and theory both have Fe features removed.

beam, smoothed by a random phase plate, strikes a gold foil. X rays from the uniform backlighting plasma are spatially imaged with 20 μm resolution, spectrally dispersed using a Hitachi 1200 lines mm^{-1} varied-line-spaced grating, and recorded on a two-dimensional image plane using a gated microchannel plate detector. The microchannel plate detector, with a CsI photocathode, is active for 100 ps at 2 ns after the heating pulse begins. The spectrometer field of view is limited to 800 μm by a beryllium aperture between the plasma and spectrometer. The spectrometer magnification is 33, and the resolving power is of order 300. The spectral coverage of the spectrometer is from 50 to 325 eV, but the signal below about 80 eV is almost entirely due to higher-order diffraction.

Figure 2 shows the image of the expanding plasma with a fully overlapped area backlight. The film optical density was measured versus position using a microdensitometer. A film calibration wedge was applied to convert from optical density to x-ray exposure. The energy calibration was then performed using the positions of observed sodium, carbon, and beryllium absorption lines. The strength of the higher-order diffraction images was obtained from the observed higher-order absorption features of beryllium and carbon. Images representing the second and third diffraction orders are normalized and subtracted from the data. Slight corrections for the second- and third-order diffraction for spectral regions above the carbon He$_\alpha$ were obtained from another data set with higher spectrometer energy coverage.

Emission and background contributions were determined from a fit based on the depths of very optically thick beryllium, carbon, and sodium transitions. The spectral shape of the background and the absence of strong line emission features were confirmed in an auxiliary shot where the sample was viewed face on with a backlight overlapping half of the sample. In this case, the image of the sample that had not been backlighted gives the emission backgrounds. With the background subtracted, the resulting image is of backlight x rays that either pass through or to the sides of the sample, and are recorded in separate locations on the multichannel plate detector. The plasma transmission is obtained by comparing the direct and attenuated x-ray signals.

The plasma density is determined from the measured width of the plasma and the known initial thickness of the foil. Iron and sodium are not uniformly mixed so that their absorption features are separately analyzed to give the individual mass distributions. The average density in the sample center is 0.0113 ± 0.001 g cm^{-3}, with a composition of 80.2 wt% iron. With the density fixed, the sodium absorption spectrum is then used to constrain the sample temperature. The technique employing the spectrum of light ionized elements has proven successful as a plasma temperature diagnostic [2,3]. The sodium transmission spectrum shown in Fig. 3 is measured at the left edge of the sample (see Fig. 2) where the sodium and fluorine absorption features are strongest. The density at the sample edge is $0.008\,36 \pm 0.0008$ g cm^{-3}, with a composition of 91 wt% NaF. The sample mass density at the edge is lower than in the center due to the greater concentration of NaF. However, the free electron densities are comparable as required for pressure equilibrium. In Fig. 3 the iron absorption features are removed using the spectrum from the sample center where the iron features are strongest but normalized to the edge iron concentration. Typical uncertainties in the transmission data are indicated in Fig. 3. Fits to the sodium data determined the ratios of the optically thin lithiumlike and berylliumlike sodium lines. For these conditions, the strength of the berylliumlike lines is reduced relative to the lithiumlike lines as temperature is increased and the sodium ionizes further. The same effect occurs with decreasing density, so an accurate density measurement is needed to determine the temperature.

The sodium spectrum was modeled using the OPAL opacity model code [8] coupled to spectroscopically accurate atomic data generated by a multiconfiguration Dirac-Hartree-Fock code (MCDF) using intermediate coupling [9]. The calculations include states from ionization sequences heliumlike through boronlike and levels with principal quantum number up to $n=7$. The ionization balance in OPAL is based on a systematic expansion of the grand canonical partition function [10]. Figure 3 shows the sodium transmission spectrum and the results of two OPAL calculations for temperatures of 57 and 59 eV. The column depth is adjusted to match the strengths of the lithiumlike transitions. Based on these fits, the inferred plasma temperature is 59 ± 3 eV. A statistical error of 1.5 eV is due to the precision with which line ratios can be determined from the data. The remaining error results from uncertainties in the sample density and modeling the spectral line shapes.

With the plasma density determined from the radiography and the plasma temperature inferred from the sodium spectrum, several predictions of the iron transmission may be compared to the data. The first model uses the supertransition array (STA) theory [11] in which all the spectral lines associated with a single-electron transition, including all possible initial and final configurations, are described by a small number of STA's whose transition energies, intensities, and variances are evaluated in optimized potentials. The second model uses a Monte Carlo unresolved transition array (MCUTA) accounting method [12], which employs a Monte Carlo sampling of configurations. Both models use *jj* coupling to compute the properties of the unresolved transition arrays and an ion sphere prescription to describe plasma effects. For the Fe calculations, the OPAL model employs a detailed term accounting (DTA) approach using parametric potentials [13] and assumes the *LS* coupling scheme for the configuration term structure.

Figure 4 shows the sample transmission data compared to the models with typical experimental uncertainties indicated at several photon energy points. The results of two STA calculations using the measured density of 0.0113 g cm^{-3} and temperatures of 57 and 59 eV are shown in Fig. 4(a) which illustrates the sensitivity of the models to temperature. The results for the MCUTA and OPAL with DTA models at the measured density and 59 eV temperature are compared to the data in Figs. 4(b) and 4(c), respectively. Note that the model spectra have not been smoothed to account for experimental resolving power.

OPAL was also used with two different approximations in the atomic physics. The first employs the detailed configuration accounting (DCA) which neglects term splitting. The second uses the same DCA method, but with the term splitting included with the unresolved transition array (UTA) approximation assuming *LS* coupling [14]. Figure 4(d) shows the OPAL model with UTA method, and Fig. 4(e) shows the OPAL model with the DCA approximation. An OPAL with DCA calculation where the computed oscillator strengths are replaced by hydrogenic values is not shown, but resembles the OPAL with DCA results in Fig. 4(e). All of the opacity models that include term broadening match the observed spectrum fairly well, although there are discrepancies in absorption coefficient as large as 60% in the spectral regions with high transmission. The OPAL with DCA calculation, which neglects term splitting, is in poor agreement with the data, and the absorption coefficient can have as much as a factor of 10 error.

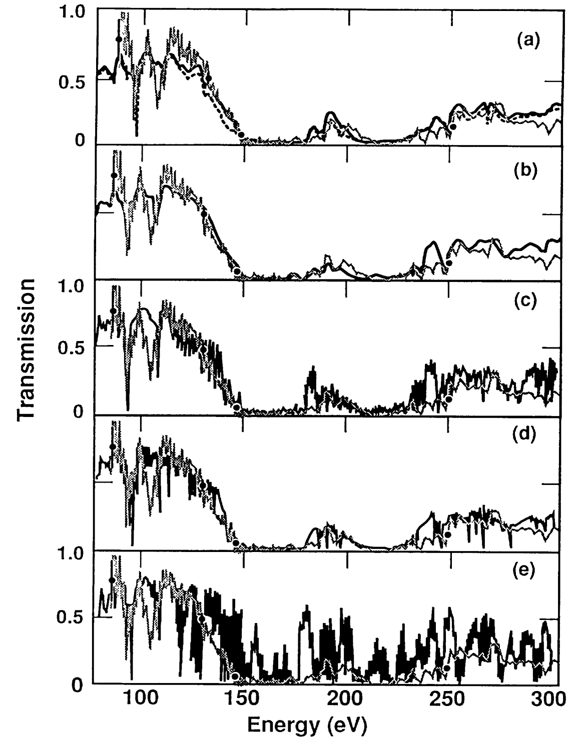

FIG. 4. Comparison of sample transmission data (gray line) and calculations for an Fe plus NaF plasma of total density 0.0113 g cm^{-3}, 80.2% by weight iron, and areal density of 339 μg cm^{-2}. (a) The STA model for temperatures of 59 eV (solid line) and 57 eV (dotted line). Remaining model calculations are for 59 eV temperature: (b) MCUTA model, (c) OPAL with DTA model, (d) OPAL with UTA model, and (e) OPAL with DCA model. The theories have not been corrected for the experimental resolution.

The transmission spectrum is converted to a frequency-dependent photoabsorption coefficient by taking the logarithm and dividing by the areal density of 339 μg cm^{-2}. The absorption coefficient was integrated with the Planck and Rosseland weighting functions in the spectral region of 100 to 300 eV. The resulting group mean opacities are given in Table I. Note that at this temperature this spectral interval encompasses the most important energy region of the weighting functions. The error estimates in the group mean opacities are due to uncertainties in the subtraction of higher-order diffraction and emission backgrounds. The experimental value of the Planck mean may be underestimated if sharp absorption features are not adequately resolved. The size of this error was estimated using smoothed model spectra to simulate experiment. Using the STA model, the experimental Planck mean is underestimated by 3%, and using the

TABLE I. Planck and Rosseland group mean opacities in $\mathrm{cm}^2\mathrm{g}^{-1}$.

	Planck	Rosseland
Experiment	8200 ± 700	4400 ± 600
STA	8431	4630
MCUTA	8226	4525
OPAL/DTA	8188	4100
OPAL/UTA	8257	4255
OPAL/DCA	8169	2997
Hydrogenic DCA	10974	2723

OPAL with DTA model, the corresponding error is 14%. Group mean opacities were computed for the models in the same spectral region as the data and the results tabulated in Table I. While there is not a large variation in Planck and Rosseland mean values predicted by the models for these conditions, the precision of the data is sufficient to distinguish the importance of term broadening in computing the Rosseland mean opacity. For this plasma, *jj* coupled models without configuration interaction perform as well as *LS* models. This finding is contrary to the results for inner-shell transitions in iron [15]. For these conditions the UTA approximations perform as well as the DTA prescription, with a considerable savings in computational effort.

Using new techniques and instrumentation, we have accurately measured the frequency-dependent absorption of a well-characterized, radiatively heated iron plasma, resulting in estimates of Rosseland and Planck group mean opacities accurate to 15%. The plasma density is determined from the spatial extent of the expanded plasma and the plasma temperature is inferred from the ionization distribution of sodium ions doped in the plasma. With plasma conditions constrained by measurements, several different opacity models are compared with the measured iron spectrum. These comparisons indicate the importance of term structure in computing both the detailed absorption spectra and the Rosseland mean opacities. The experiment also demonstrates the accuracy of several opacity models having a variety of approximations in the atomic physics, equation of state, and computational methodology.

We would like to thank C. Bruns and J. Emig for helping assemble the experiment, J. Ticehurst for her help with the analysis, R. Wallace for his assistance in target preparation, and the NOVA crew for operating the laser. This work was performed under the auspices of the U.S. Department of Energy by the Lawrence Livermore National Laboratory under Contract No. W-7405-ENG-48.

[1] *Radiative Properties of Hot Dense Matter*, edited by W. Goldstein, C. Hooper, J. Gautier, J. Seely, and R. Lee (World Scientific, Singapore, 1991).
[2] T. S. Perry *et al.*, Phys. Rev. Lett. **67**, 3784 (1991).
[3] P. T. Springer *et al.*, in *Atomic Processes in Plasmas*, edited by E. S. Maramar and J. L. Terry (AIP, New York, 1991), p. 78.
[4] J. M. Foster *et al.*, Phys. Rev. Lett. **67**, 3255 (1991).
[5] S. J. Davidson *et al.*, Appl. Phys. Lett. **52**, 847 (1988).
[6] J. Bruneau *et al.*, Phys. Rev. A **44**, 832 (1991), and references therein.
[7] L. Da Silva *et al.*, Phys. Rev. Lett. **69**, 438 (1992).
[8] F. J. Rogers and C. A. Iglesias, Astrophys. J. Suppl. **79**, 507 (1992).
[9] I. P. Grant *et al.*, Comput. Phys. Commun. **21**, 207 (1980); B. J. McKenzie *et al.*, Comput. Phys. Commun. **21**, 233 (1980); M. H. Chen, Phys. Rev. A **31**, 1449 (1985).
[10] F. J. Rogers *et al.*, Astrophys. J. **310**, 723 (1986), and references therein.
[11] A. Bar-Shalom *et al.*, Phys. Rev. A **40**, 3183 (1989); A. Bar-Shalom *et al.*, in *Atomic Processes in Plasmas* (Ref. [3]), p. 68.
[12] B. G. Wilson *et al.*, in *Atomic Processes in Plasmas* (Ref. [3]), p. 189.
[13] F. J. Rogers, B. G. Wilson, and C. A. Iglesias, Phys. Rev. A **38**, 5007 (1988).
[14] C. Bauche-Arnault, J. Bauche, and M. Klapish, Adv. At. Mol. Phys. **23**, 131 (1988).
[15] P. T. Springer *et al.* (to be published).

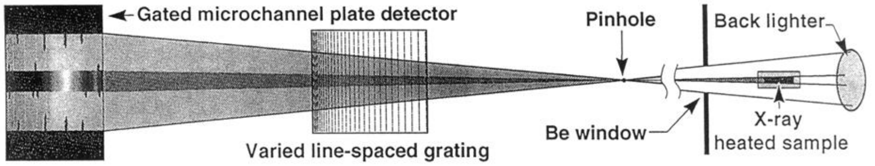

FIG. 1. Schematic drawing of the experimental setup. The radiatively heated Fe plus NaF sample is viewed edge on with the XUV spectrometer, with pinhole imaging, a gated microchannel plate detector, and is backlighted by a laser irradiated gold foil. X rays that pass through and to the side of the plasma are compared to obtain the plasma transmission.

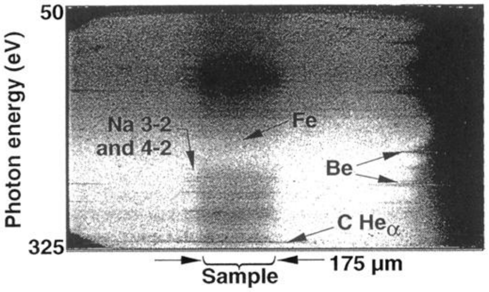

FIG. 2. Spatially resolved (left to right) and spectrally dispersed from 50 to 325 eV (top to bottom) x-ray transmission image of the Fe/NaF sample. Iron $n=3$ to $n=4$ and 5 absorption features appear in the image center as dark bands traversing the plasma. The sodium and fluorine lines are most clearly visible on the left-hand edge of the sample. Beryllium and carbon lines are also observed from the aperture and the Lexan tamper.

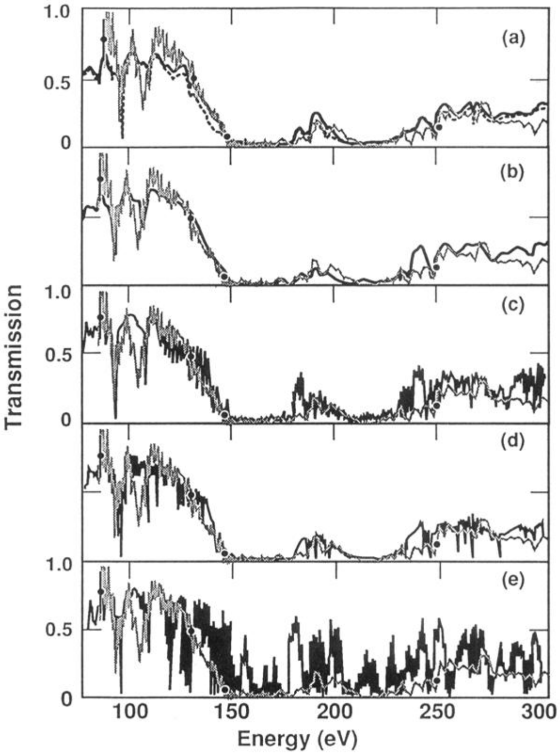

FIG. 4. Comparison of sample transmission data (gray line) and calculations for an Fe plus NaF plasma of total density 0.0113 g cm^{-3}, 80.2% by weight iron, and areal density of 339 $\mu\text{g cm}^{-2}$. (a) The STA model for temperatures of 59 eV (solid line) and 57 eV (dotted line). Remaining model calculations are for 59 eV temperature: (b) MCUTA model, (c) OPAL with DTA model, (d) OPAL with UTA model, and (e) OPAL with DCA model. The theories have not been corrected for the experimental resolution.